



# Analysis of ionosphere response during high-speed solar wind stream in early August 2020

Jie Li<sup>1</sup> · Shuqing Wang<sup>1</sup> · Shuhui Li<sup>1</sup> · Zifan Xu<sup>1</sup> · Jun Yang<sup>1</sup>

Received: 9 April 2021 / Accepted: 19 June 2021 / Published online: 4 August 2021  
© The Author(s), under exclusive licence to Springer Nature B.V. 2021

**Abstract** Ionosphere parameters obtained from International Global Navigation Satellite System (GNSS) Service (IGS) stations and SWARM satellites were used to analyze ionosphere response during high-speed solar wind stream (HSSWS) in early August 2020. The ionosphere total electron content (TEC) and the rate of TEC index (ROTI) were calculated from August 1 to 8 2020. The ionosphere parameters in different regions showed an abnormal increase or decrease, but latitude differences were observed and different types of data had different characteristics of abnormal changes. ROTI values in high-latitude areas were six times that in low-latitude areas, and the occurrence rate of ROTI>0.5 reached approximately 54%. The electron density of the topside ionosphere increased by up to 15% during HSSWS. The most affected area was the European–African continent, and the electron density increased by approximately 104%. SWARM TEC also produced a large disturbance, and ROTI reached a peak of 1.77 TECU/min. In addition, ionosonde data were used to detect TEC changes of the lower ionosphere of the F2 layer. Results show that the positive and negative disturbances of the TEC and foF2 parameters existed. The disturbance of ionosonde TEC became considerably larger when the GNSS TEC increased.

**Keywords** HSSWS · TEC · ROTI · SWARM · Ionosondes

## 1 Introduction

Solar wind is a supersonic plasma-charged particle stream emitted from the upper atmosphere of the Sun (Krieger et al.

1973; Nolte et al. 1976). The charged particles may damage the Earth's satellites and electric power system and affect the ozone layer and wireless communication when the wind speed reaches more than 800 km/s. The solar wind is vital to understand the inner dynamics of the Sun. It is also an important study field for investigating the ionosphere response to solar wind.

Many scholars have studied the ionosphere response using GNSS observations during HSSWS (Rodríguez-Zuluaga et al. 2016; Watson et al. 2016; Liu et al. 2019). After accelerating the solar wind, the southward components of interplanetary Alfvén waves are reconnected with the interplanetary magnetic field (IMF) to transfer solar wind energy to the magnetosphere (Liu et al. 2020). Therefore, the intensity of geomagnetic activity depends on the southward magnetic component Bz (Tsurutani et al. 2018; Matamba and Habarulema 2020). The interaction between HSSWS and the magnetosphere produces prompt penetrating electric fields (PPEFs), whose amplitude is directly affected by the interplanetary electric field (IEF). The impact of HSSWS on the ionosphere is closely related to PPEFs, thereby strengthening the positive or negative storms in the ionosphere (Sulungu and Uiso 2019). During the recovery phase of the geomagnetic storm, HSSWS eventually causes the auroral ellipse and low latitude areas to increase by 2 TECU (Ren et al. 2020). Corotating interaction regions (CIRs) generated by the interaction between interplanetary coronal mass ejections (ICMEs) and high-speed stream (HSS) cause the strong geomagnetic storm in low-latitude regions (Bu et al. 2019; Molina et al. 2020). Zaourar et al. (2017) studied the interhemispheric conjugated behavior and found that the ionosphere TEC amplitude in the northern hemisphere is greater. The asymmetry is stronger at high latitudes during HSSWS.

✉ S. Wang  
w\_sq\_2002@163.com

<sup>1</sup> School of Land Science and Technology, China University of Geosciences (Beijing), Beijing 100083, China

Many results have been obtained in the study of the ionosphere response to HSSWS by using in-situ measurements. Satellites generally obtain electron density by installing Langmuir probes (LPs). The data of LPs onboard CHAMP indicate that the position variation of the ionosphere mid-latitude trough is mainly affected by the dawn-dusk component of solar wind electric field (Liu et al. 2015). Liou et al. (2013) studied ionosphere response to solar wind pressure pulses under northward IMF conditions. They concluded that the solar wind pressure pulse is an important cause of geomagnetic activity in the northern component of the IMF.

In recent years, low Earth orbit (LEO) Global Positioning System (GPS) technology has also been widely used in space weather analysis and research; its reliability in measuring topside ionosphere disturbances has been confirmed. Although the data of the GPS receivers onboard LEO satellites have similarities to the in-situ measurement data, they cannot substitute each other (Zakharenkova and Astafyeva 2014).

Contrary to other single LEO satellites, the SWARM satellite is composed of three near-polar orbit satellites. The ionosphere variations of different longitudes and altitudes can be compared. In addition, the SWARM satellite has higher temporal resolution. Therefore, it can provide a large amount of data to study the changes in the topside ionosphere.

Previous studies have conducted abundant analysis on the ionosphere response during HSSWS. However, further comprehensive analysis of ground-based GNSS, GPS receiver onboard SWARM satellite, and in situ measurement data will contribute to the understanding of the ionosphere response characteristic during HSSWS. Ionosphere disturbances are very complex phenomena in the upper atmosphere. Analyzing the ionosphere response under more high-speed solar wind events is also meaningful for investigating the changes in the Earth's space environment. Ground-based GNSS station data, SWARM satellite, and ionosonde data were used to analyze the ionosphere disturbance characteristics under the high-speed solar wind event in early August 2020. The percentage of changes in various observations was calculated. The results obtained are important reference for further research on response mechanisms.

## 2 Data and methods

The ionosphere changes during the HSSWS from August 2 to 6 2020 were studied. The solar wind speed continued to rise since 03:30 UT on August 2 and reached a peak of 733.7 km/s at 03:49 UT on August 4. For the first time, the solar wind speed reached 700 km/s since 2020. Other solar activities were relatively gentle, and the ionosphere was less affected by other solar activities.

Six types of data were used in this experiment, as follows: (1) ground-based GNSS data are obtained from the Crustal Dynamic Data Information System (<ftp://cddis.gsfc.nasa.gov/gps/data/daily/>). It is used to calculate the TEC and ROTI and the time resolution is 30 s. (2) The final product of Global Ionospheric Maps (GIMs) is provided by IGS (<ftp://cddis.nasa.gov/gnss/products/ionex/>) and used to simulate the global ionosphere response. The spatial resolution in geographic latitude and longitude is  $2.5^\circ \times 5^\circ$ , and the time resolution is 2 h. (3) In situ measurement data of SWARM satellite ([ftp://swarm-diss.eo.esa.int/Level1b/Entire\\_mission\\_data/EFIx\\_LP/](ftp://swarm-diss.eo.esa.int/Level1b/Entire_mission_data/EFIx_LP/)) are used to detect the plasma density in the topside ionosphere, and the time resolution is 2 s. (4) LEO GPS data ([ftp://swarmdiss.eo.esa.int/Level2daily/Entire\\_mission\\_data/TEC/TMS/](ftp://swarmdiss.eo.esa.int/Level2daily/Entire_mission_data/TEC/TMS/)) are used to calculate TEC and ROTI in the topside ionosphere. (5) The ionosonde data (<http://giro.uml.edu/didbase/scaled.php>) include F2 layer critical frequency foF2 and bottom side TEC values. (6) In addition, the data describing solar activities and geomagnetic indices are obtained from the OMNI data website (<https://omniweb.gsfc.nasa.gov/>), including the global daily geomagnetic variation Kp, the disturbance storm time Dst, the amplitude of IMF, and IMF southward component.

IGS stations were selected to represent high-, mid-, low-latitude, and equatorial regions. Five ionosonde stations were located in the American continent, European–African continent, and Asian–Australian continent. As shown in Fig. 1, these stations are evenly distributed worldwide. The geographic coordinates of the selected ionosonde stations and IGS stations are listed in Table 1.

We calculated the ionosphere slant TEC (STEC) from the dual-frequency GPS observation data (Jin et al. 2012). The equation is as follows:

$$P_4 = P_1 - P_2 = I_1 - I_2 + DCB_r + DCB^s \quad (1)$$

$$\begin{aligned} L_4 &= L_1 - L_2 \\ &= -(I_1 - I_2) + \lambda_1 N_1^s - \lambda_2 N_2^s + \lambda_1 B_{r,1}^s + \lambda_2 B_{r,2}^s \end{aligned} \quad (2)$$

where  $P_1$  and  $P_2$  represent the pseudorange measurements;  $L_1$  and  $L_2$  represent the carrier phase observations;  $I_1$  and  $I_2$  indicate the ionospheric delay;  $DCB_{r,1,2}$  and  $DCB_{1,2}^s$  are differential code bias (DCB) of the receiver and satellite, respectively;  $\lambda_1$  and  $\lambda_2$  represent the wave lengths of the dual-frequency signal;  $N_1^s$  and  $N_2^s$  indicate the ambiguity;  $B_{r,1}^s$  and  $B_{r,2}^s$  indicate the biases between the satellite and the receiver.

The pseudorange observations  $P_4$  have larger noise; thus, the carrier phase-smoothed pseudorange is used to obtain smoothed  $P_4^\Delta$  observations. The equation is as follows:

$$P_{4,k}^\Delta = \omega P_{4,k} + (1 - \omega)(P_{4,k-1}^\Delta + (L_{4,k} + L_{4,k-1})) \quad (3)$$

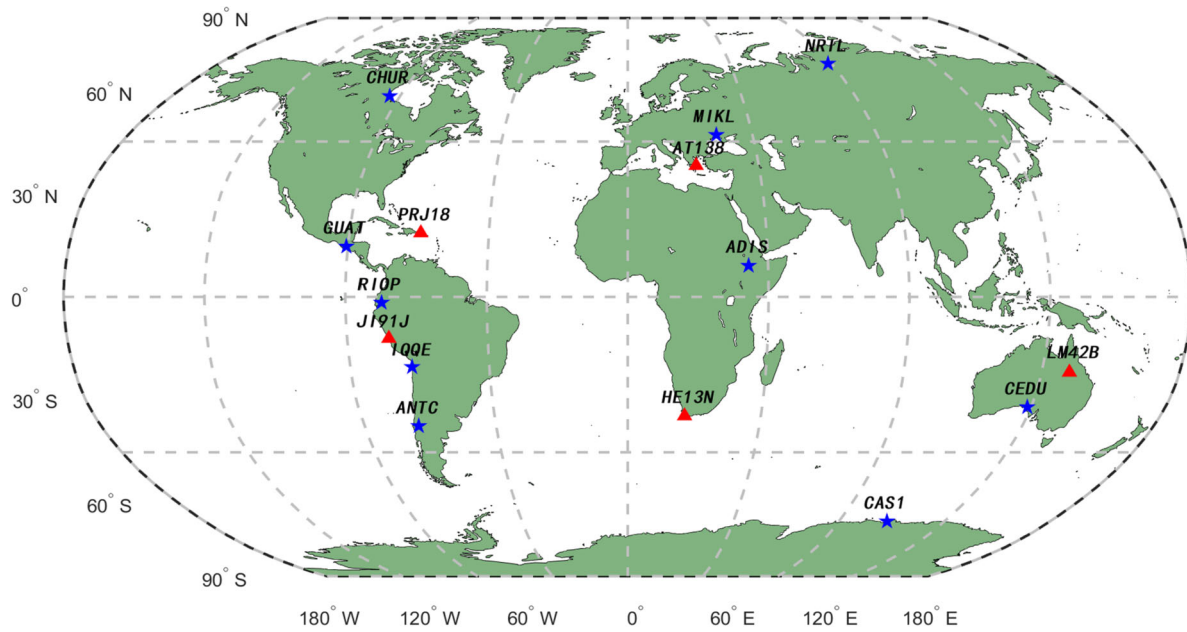


**Fig. 1** GNSS and ionosonde stations used: the blue stars indicate IGS stations, the red triangles are ionosonde stations, and all the dashed lines show the geographic latitude and longitude lines

**Table 1** Geographical coordinates of test stations

Name of test stations	Type of test stations	Geographic longitude (deg)	Geographic latitude (deg)
Nril	IGS	88.36	69.36
Chur	IGS	265.91	58.76
Mikl	IGS	31.97	46.97
Guat	IGS	269.48	14.59
Adis	IGS	38.77	9.04
Riop	IGS	281.35	-1.65
Iqqe	IGS	289.87	-20.27
Cedu	IGS	133.81	-31.87
Antc	IGS	288.47	-37.34
Cas1	IGS	110.52	-66.28
AT138	Ionosonde	23.50	38.00
PRJ18	Ionosonde	292.90	18.50
JI91J	Ionosonde	283.20	-12.00
LM42B	Ionosonde	144.10	-21.80
HE13N	Ionosonde	19.22	-34.42

$$P_{4,k}^{\Lambda} = -40.3 \cdot \left( \frac{1}{f_1^2} - \frac{1}{f_2^2} \right) \cdot STEC_k + DCB_{r,k} + DCB_k^s \tag{4}$$

where  $P_{4,k}^{\Lambda}$  represents the carrier phase-smoothed pseudorange at epoch  $k$ ;  $\omega$  is the weight factor, and  $\omega = 0.5$ ;  $f_1$  and  $f_2$  are the carrier frequencies of the dual-frequency signal.

Then, STEC can be converted to TEC in the vertical direction by using the projection function  $MF(z)$  (Beutler

et al. 1999).  $MF(z)$  is obtained as follows:

$$MF(z) = \cos \left( \arcsin \left( \frac{R}{R+H} \sin(\alpha z) \right) \right) \tag{5}$$

where  $R = 6371$  km is the average radius of the Earth;  $H$  is the average height of the puncture point, and in this case,  $H = 375$  km;  $\alpha = 0.9782$ ;  $z$  represents the zenith angle.

Furthermore, the rate of TEC (ROT) and the ROT index (ROTI) are computed. ROT is the rate of change of slant

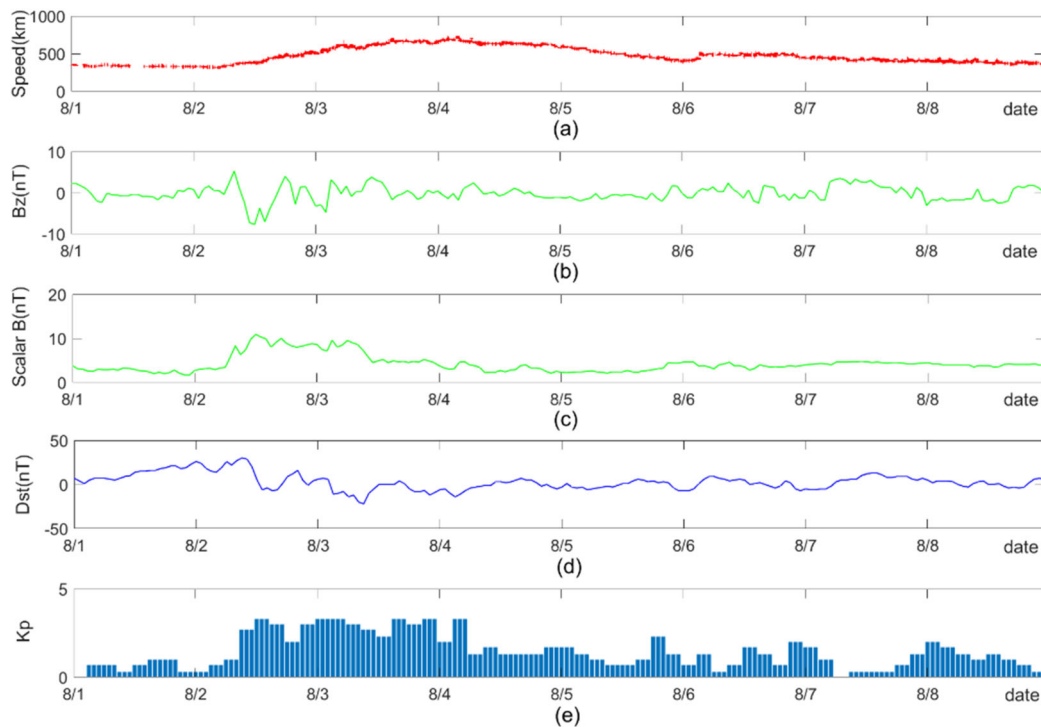


**Fig. 2** Solar and geomagnetic indices during HSSWS in 2020, (a) is solar wind speed, in (b) and (c) IMF Bz and scalar are shown; Dst and Kp are demonstrated in (d) and (e)

TEC. ROTI is the standard deviation of the time-varying ROT (Pi et al. 1997). ROTI is usually used as an important indicator to detect the presence of ionosphere irregularities. ROT and ROTI can be obtained using the following equation:

$$ROT = \frac{STEC_{k+1} - STEC_k}{\Delta t_k} \quad (6)$$

$$ROTI = \sqrt{\frac{1}{N} \sum_{j=1}^N (ROT_j - ROT_{aver})^2} \quad (7)$$

where  $STEC_k$  represents the STEC at epoch  $k$ ;  $\Delta t_k$  represents the interval; the unit of ROT and ROTI is TECU/min;  $ROT_j$  and  $ROT_{aver}$  represent the ROT at epoch  $j$  epoch and the averaged ROT of  $N$  epochs, respectively;  $N = 10$ .

### 3 Results and discussion

#### 3.1 Solar and geomagnetic indices during HSSWS event in early August 2020

Variations of the solar and geomagnetic indices in early August 2020 are demonstrated in Fig. 2. The speed of solar wind has continued to increase since August 2. It lasted for four days at a speed above 500 km/s and finally dropped to

400 km/s on August 7. The HSSWS caused the oscillation of the interplanetary magnetic field. The IMF Bz increased to 5.4 nT after 06:00 UT on August 2. Subsequently, it decreased to  $-7.7$  nT and returned to normal at 15:00 UT on August 3. In terms of the changes in the geomagnetic index, the Kp index suddenly increased from 1 to 2.7 after 08:00 UT on August 2. It continued to become higher than 2 for the next two days. The HSSWS causes the oscillation of the interplanetary magnetic field, further affecting the global geomagnetic activity.

#### 3.2 Ionosphere changes detected by ground-based GNSS data

GIMs data at longitudes  $70^\circ$  W,  $20^\circ$  E, and  $130^\circ$  E were used to represent the ionosphere over the American continent, European–African continent, and Asian–Australian continent, respectively. The ionosphere TEC over the three regions showed a significant increase since August 2. In summary, the region most affected by HSSWS is the European–African continent, where ionosphere TEC increased by 12%. The area with the most significant ionosphere response is  $20^\circ$  E and  $35^\circ$  S, with a variable percentage of 68%. TEC over American continent and Asian–Australian continent has changed by 11% and 10%, respectively. The ionosphere around the equator has an evident equatorial ionization anomaly (EIA) phenomenon, which is mainly caused

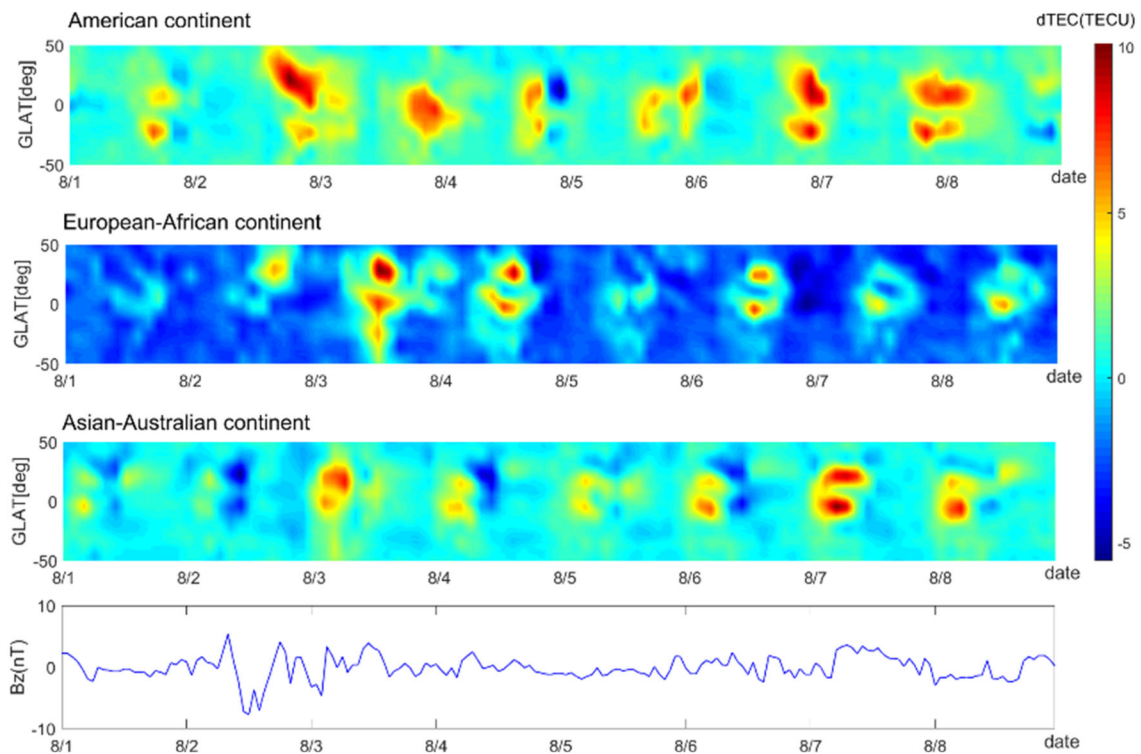


**Fig. 3** Differences between observed TEC and reference values over the American continent, European–African continent, and Asian–Australian continent during HSSWS in 2020

by the fountain effect. After approximately 0:00 UT on August 7, a new round of ionosphere oscillation emerged in the American continent and the Asian–Australian continent.

The differences between the observed ionosphere TEC and reference values over the American continent, European–African continent, and Asian–Australian continent are shown in Fig. 3. The change rates of TEC over three regions are drawn in Fig. 4. The averaged TEC under quiet geomagnetic conditions (July 26 to 31) were considered the reference values. These figures show a more evident EIA phenomenon at low latitudes, as well as the hemispheric asymmetry of the ionosphere response. The ionosphere TEC over the equatorial area of the north American continent increased by 60% at 17:30 UT on August 2, and the TEC at the conjugate location in the southern hemisphere did not change substantially. The ionosphere over the 130° E and 50° S area south of Australia increased to 88% at 16:00 UT on August 2. However, the TEC at the conjugate location in the northern hemisphere only changed by 8%.

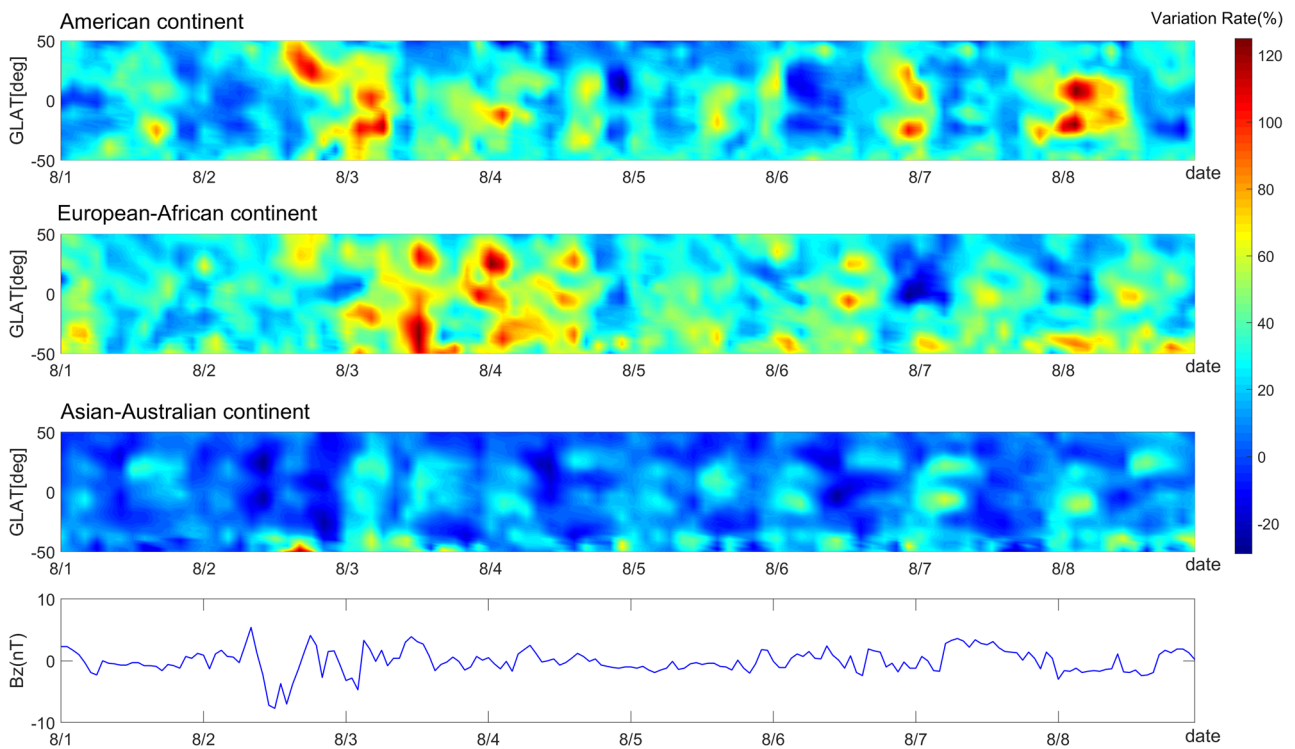
Figure 5 plots the ionosphere disturbance index ROTI over different IGS stations. The figure shows the amplitudes of ROTI in the northern hemisphere were greater than the southern hemisphere during HSSWS. The ROTI of Nril station reached a peak of 4.92 TECU/min, which was four to five times that of a quiet period. To further explore the relationship between ionosphere disturbances and latitude, we

calculated the occurrence rate of ROTI. As shown in Fig. 6, the strong ionosphere disturbances at high latitude stations in the northern hemisphere appeared after 14:00 UT on August 2. The occurrence rate of  $\text{ROTI} > 0.5$  at Nril station and Chur station even reached 48% and 54%, respectively. The occurrence rate of  $\text{ROTI} > 0.3$  at high latitude stations was significantly higher than at low latitude stations.

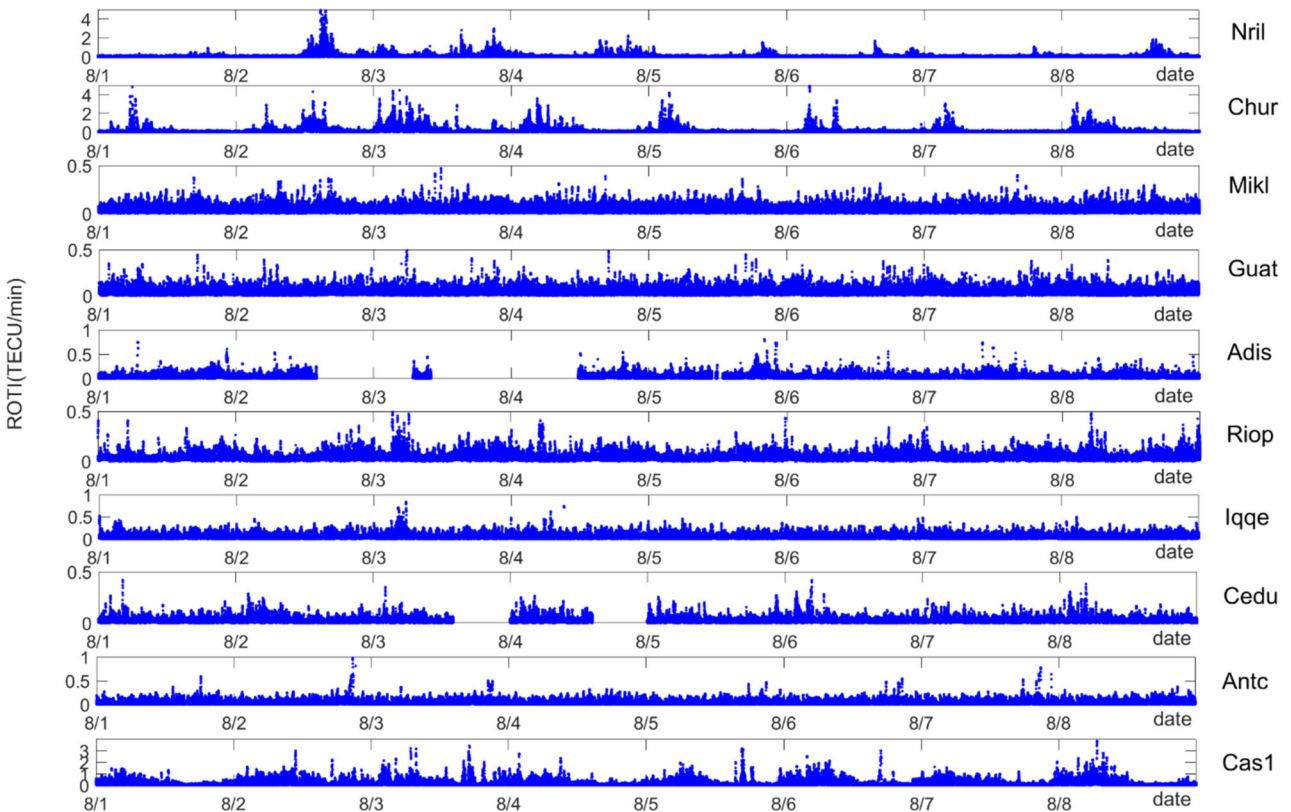
### 3.3 Ionosphere changes detected by SWARM satellite

Figure 7 shows the variation of the global electron density  $N_e$  in the topside ionosphere during HSSWS. Table 2 shows the statistics of global electron density  $N_e$  changes. The reference values are the averaged  $N_e$  from July 26 to 31. The table shows that the ionosphere electron density near the equator had a clear upward trend on August 3, with an average increase rate of 15%. It finally returned to normal on August 7. It was eight times that of the geomagnetic quiet period when the increment of electron density reached its peak. It occurred at 81.1° E and 19.4° N. In addition, the electron density of the topside ionosphere had a spatial distribution pattern. Compared with low-latitude regions, the electron density changes in high-latitude regions are not evident.

Figure 8 depicts the changes in the topside ionosphere electron density over the American continent, European–



**Fig. 4** Change rate of ionosphere TEC over the American continent, European–African continent, and Asian–Australian continent during HSSWS in 2020



**Fig. 5** Ionosphere ROTI calculation results of IGS stations during HSSWS in 2020

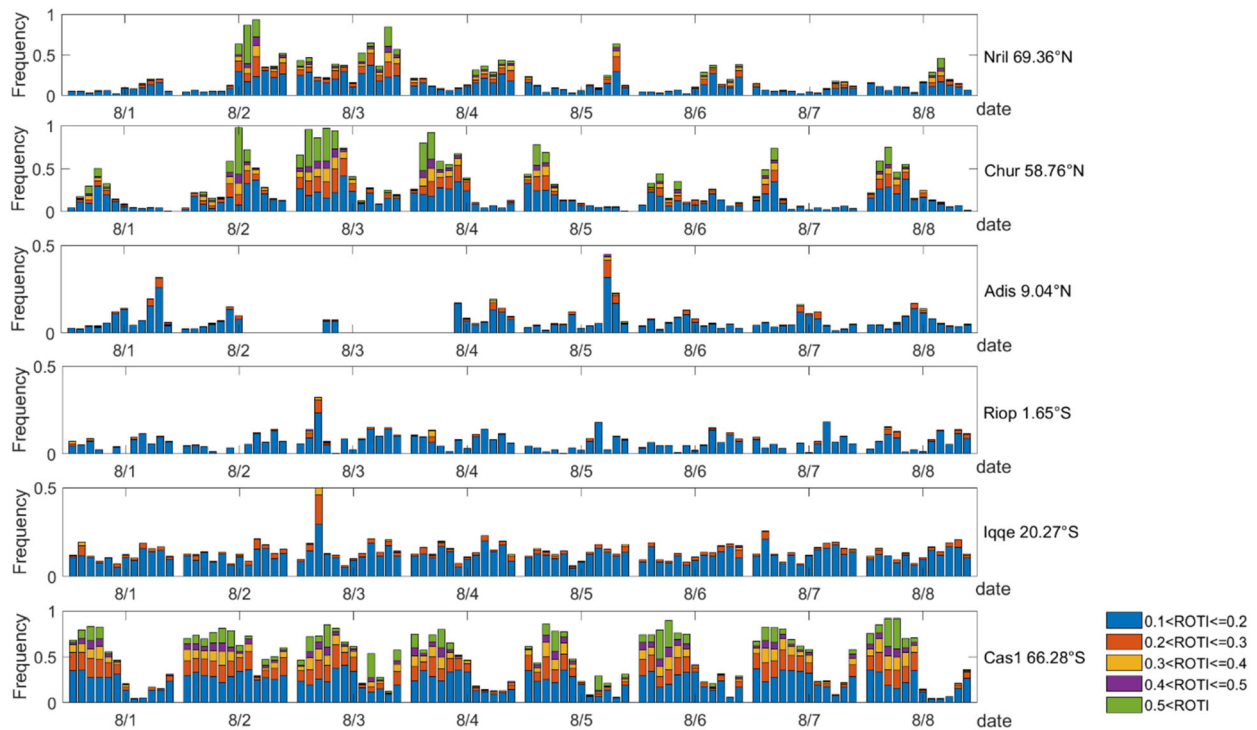


**Fig. 6** Statistics of ROTI occurrence rate at different latitude IGS stations during HSSWS in 2020

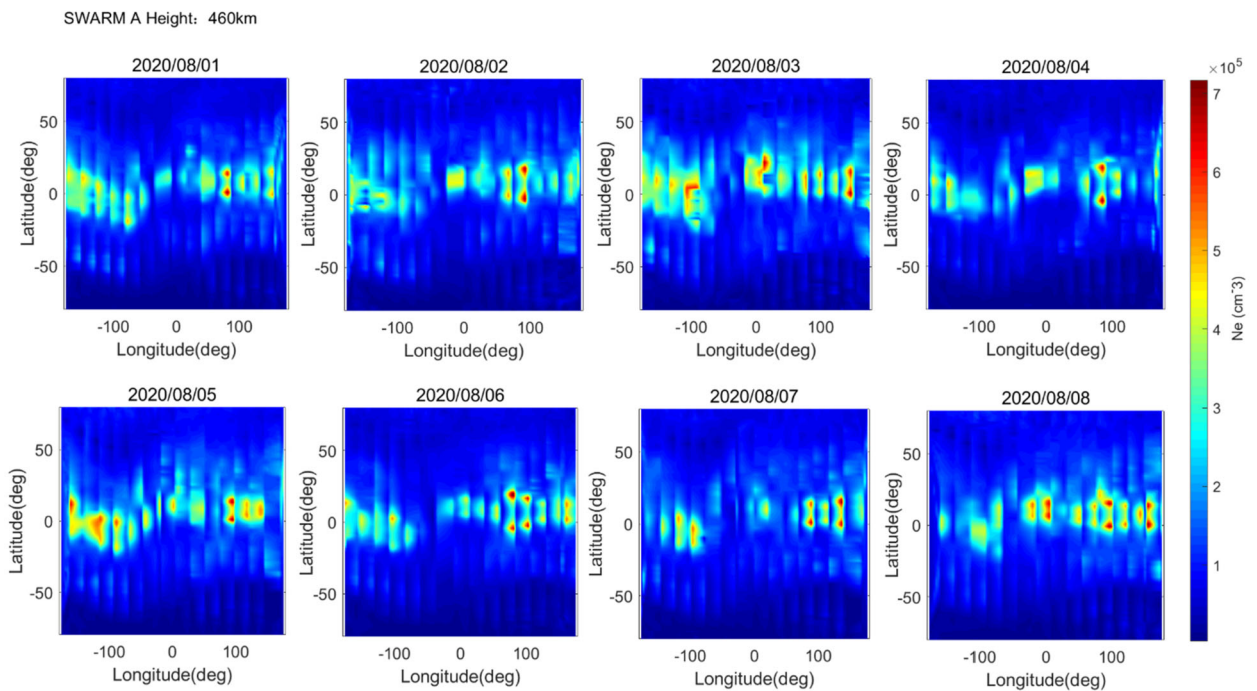


**Fig. 7** Global electron density Ne change based on SWARM A satellite data during HSSWS in 2020

African continent, and Asian–Australian continent during HSSWS. The electron density of the topside ionosphere increased on August 3, thereby corresponding to the positive storm of the solar wind. The EIA phenomenon appeared

near the equator during HSSWS. The topside ionosphere of the European–African continent was most affected, with an average increase rate of 104% on August 3. The peak electron density near 148.5° E and 0.5° N could be up to four

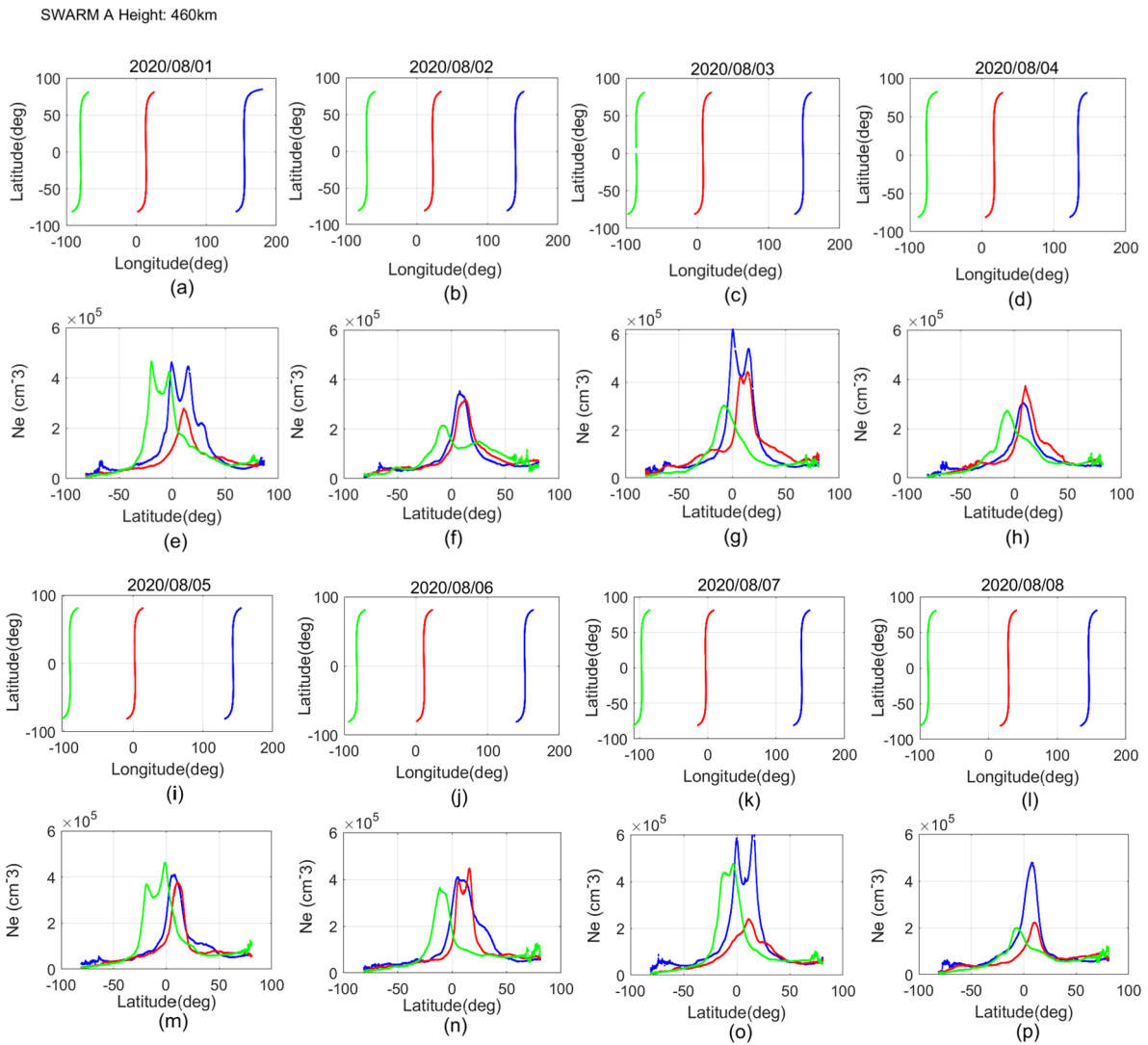


**Fig. 8** Electron density Ne changes over the American continent, European–African continent, and Asian–Australian continent during HSSWS in 2020, (a)–(d) and (i)–(l) are the flight trajectories of the SWARM A satellite, (e)–(h) and (m)–(p) show the electron density Ne

**Table 2** Statistics of global electron density Ne changes from SWARM A satellite during HSSWS in 2020

Date	Average of bias between Ne and reference values ( $10^5 \text{ cm}^{-3}$ )	Max. of bias between Ne and reference values ( $10^5 * \text{cm}^{-3}$ )	Average increase rate of Ne (%)
2020/08/01	0.04	3.76	4
2020/08/02	0.07	4.63	11
2020/08/03	0.12	4.18	15
2020/08/04	0.04	5.81	4
2020/08/05	0.01	2.62	2
2020/08/06	0.06	5.11	7
2020/08/07	−0.03	4.76	1
2020/08/08	0.04	4.02	7



**Fig. 9** VTEC and ROTI variation with latitude based on SWARM A satellite during HSSWS in 2020; green, red, and blue solid lines represent TEC over American continent, European–African continent, and Asian–Australian continent, respectively. The green, red, and blue solid points represent the ROTI over the three continents

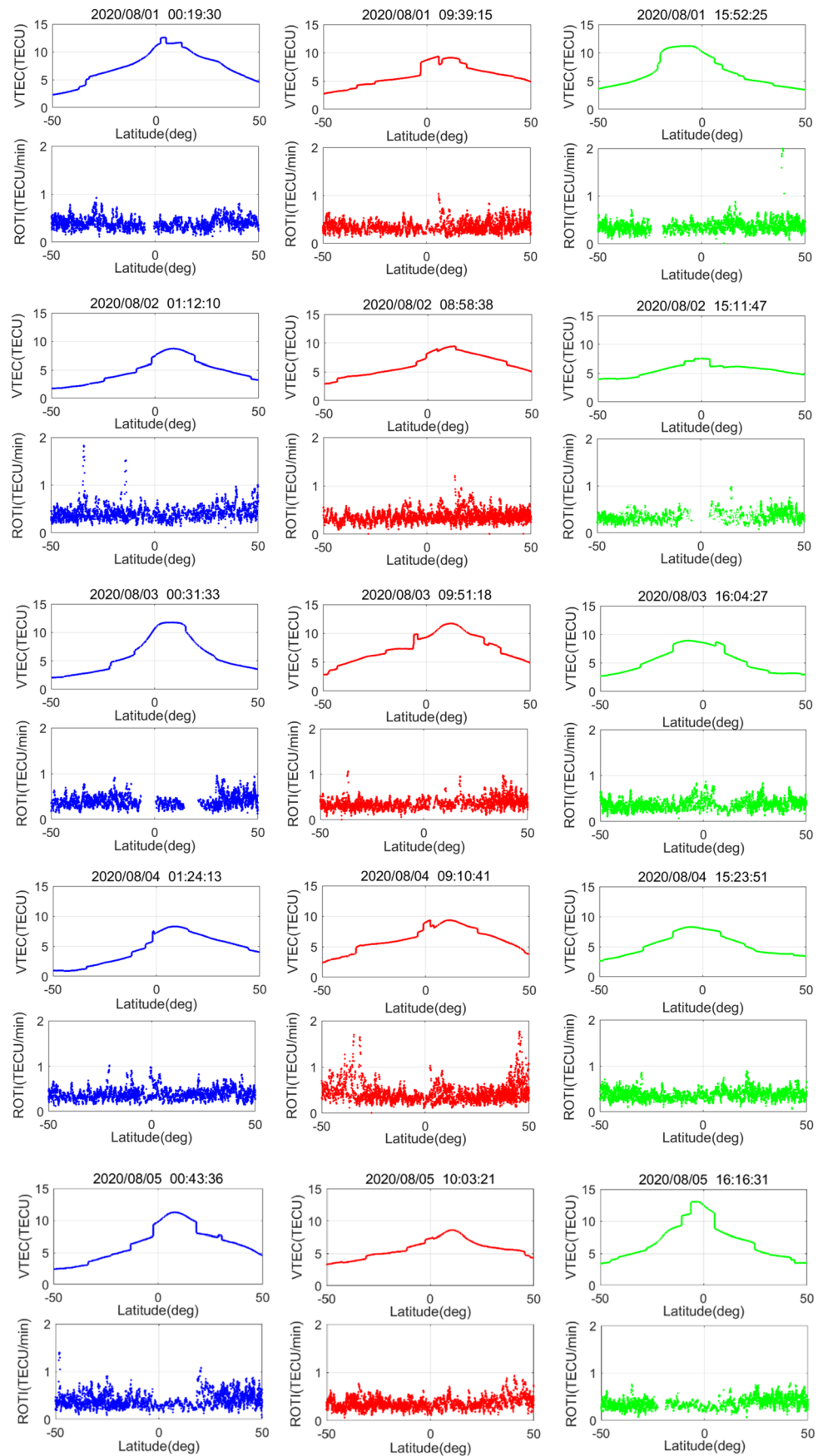
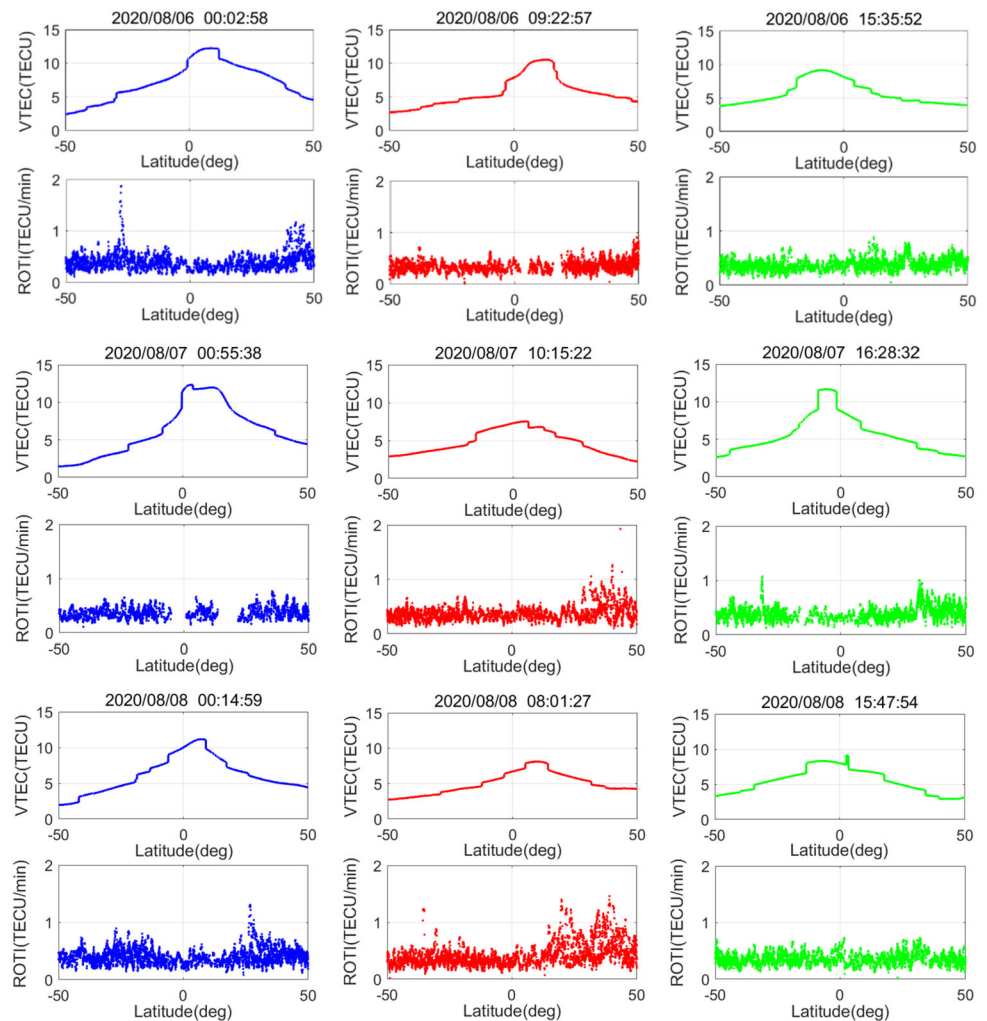


Fig. 9 (Continued)



times higher than usual. The electron density of the Asian–Australian continent increased by 81%, and the maximum was five times higher than usual.

The ionosphere LEO VTEC and LEO ROTI changes during HSSWS were calculated, as shown in Fig. 9. To compare with the in-situ measurement results, we selected ionosphere VTEC over the American continent, European–African continent, and Asian–Australian continent. The data were received from the same satellite at the same time. The electron density measured by LP and LEO TEC technology are similar. However, the two data sets are not the same (Zakharenkova and Astafyeva 2014). After August 1, the peaks of TEC and ROTI in the three regions had an upward trend. The ionosphere disturbance over the European–African continent increased significantly. The ROTI of the topside ionosphere is greater at high latitudes. This finding is similar to the spatial variation results obtained from the GNSS observations.

Figure 10 displays the ROTI occurrence rate over the three regions during HSSWS. From August 2, the occurrence rate of  $\text{ROTI} > 0.5$  has increased evidently over the

American continent and Asian–Australian continent. However, in the European–African continent, the occurrence rate of  $\text{ROTI} > 0.5$  increased more significantly on August 3 and 4. The occurrence rate of  $\text{ROTI} > 0.5$  in the American continent and Asian–Australian continent was 27% and 26%, respectively.

### 3.4 Ionosphere changes detected by ionosonde data

The TEC at the bottom of the F2 layer can be obtained by ionosondes. Five ionosonde stations located in the American continent, European–African continent, and Asian–Australian continent were selected. Figures 11–15 exhibit the variation of foF2, TEC, and tROTI of stations. The tROTI was obtained by calculating the TEC change rate of adjacent epochs. The reference values are the averaged values of foF2 and TEC from July 26 to 31. Table 3 shows the statistics of foF2 and TEC from ionosonde stations. Compared with the ionosphere under quiet conditions, the peaks

**Fig. 10** Statistics of ROTI occurrence rate over the American continent, European–African continent, and Asian–Australian continent during HSSWS in 2020

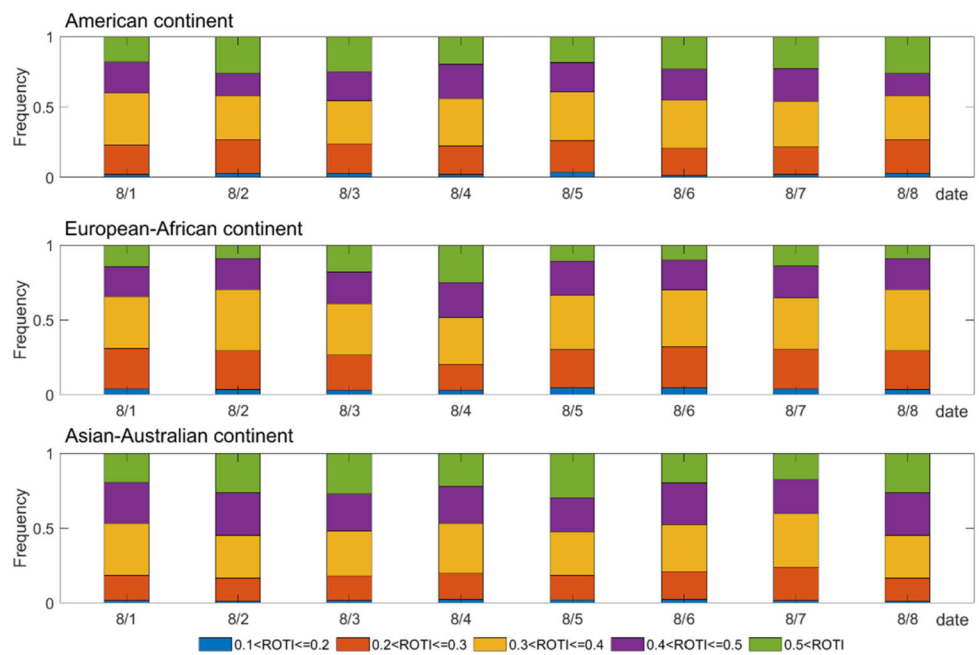
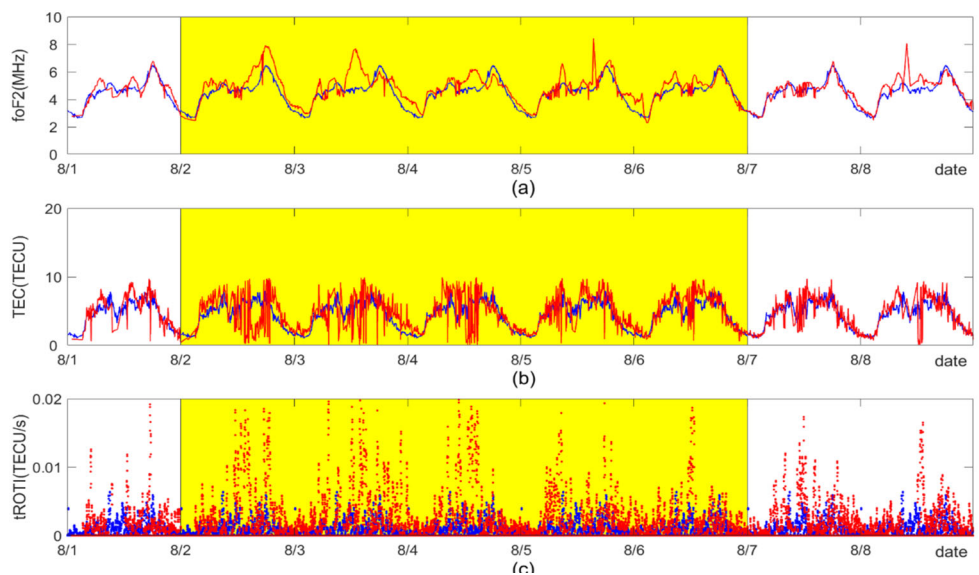


**Fig. 11** Ionosphere foF2 and TEC derived from AT138 station during the HSSWS in 2020 (a) foF2, (b) TEC, and (c) tROTI; solid blue lines represent the reference values of foF2 and TEC, solid red lines represent the observations, and yellow paddings show the period of the HSSWS event



of foF2 and the TEC of the bottom ionosphere have an increasing trend after August 1. The figure shows that the larger values of tROTI appeared more densely after August 2. Among the five stations, HE13N station located in southern Africa was most affected by HSSWS. The ionosphere foF2 and TEC over HE13N station increased by 12% and 32%, respectively. The ionosphere disturbance over higher latitude stations was evidently stronger during HSSWS in 2020.

Figure 16 plots the ionosphere TEC changes on five ionosonde stations by using GNSS, SWARM, and ionosonde data during HSSWS. The SWARM A satellites pass verti-

cally over the stations only on certain days. Therefore, we selected the data whose difference between the SWARM satellites and the ionosonde stations is within 3° in geographic longitude and latitude. The figure shows that the ionosphere response obtained from GNSS data were the strongest. The average increase rate at HE13N station was 97%. SWARM TEC and ionosonde TEC have the same amplitude of oscillation. The variations of TEC from GNSS and ionosonde had temporal consistency which was particularly evident in mid-latitude stations. The bottom ionosphere disturbance increased almost simultaneously when the GNSS TEC increased.

**Fig. 12** Ionosphere foF2 and TEC derived from PRJ18 station during the HSSWS in 2020 (a) foF2, (b) TEC, and (c) tROTI; solid blue lines represent the reference values of foF2 and TEC, solid red lines represent the observations, and yellow paddings show the period of the HSSWS event

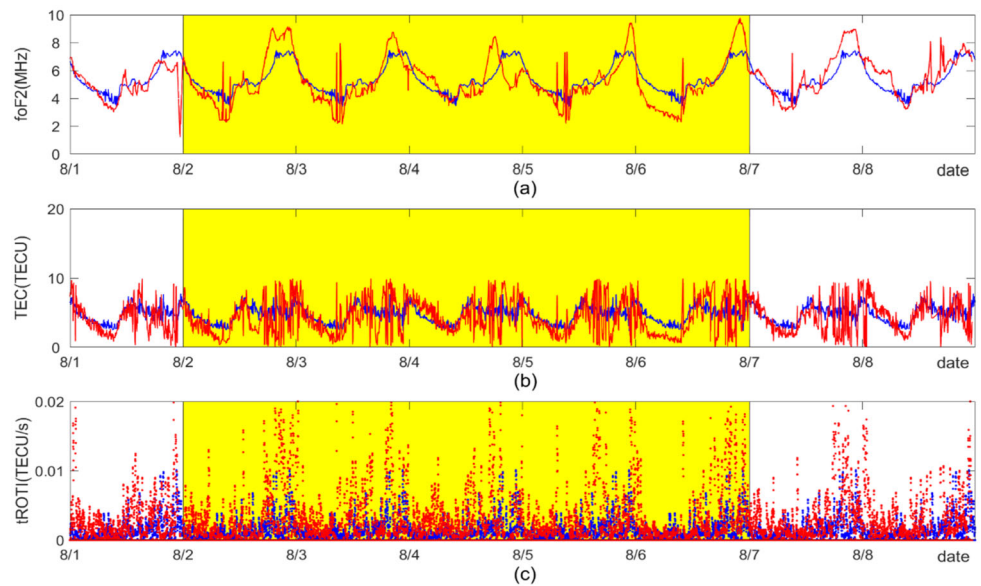
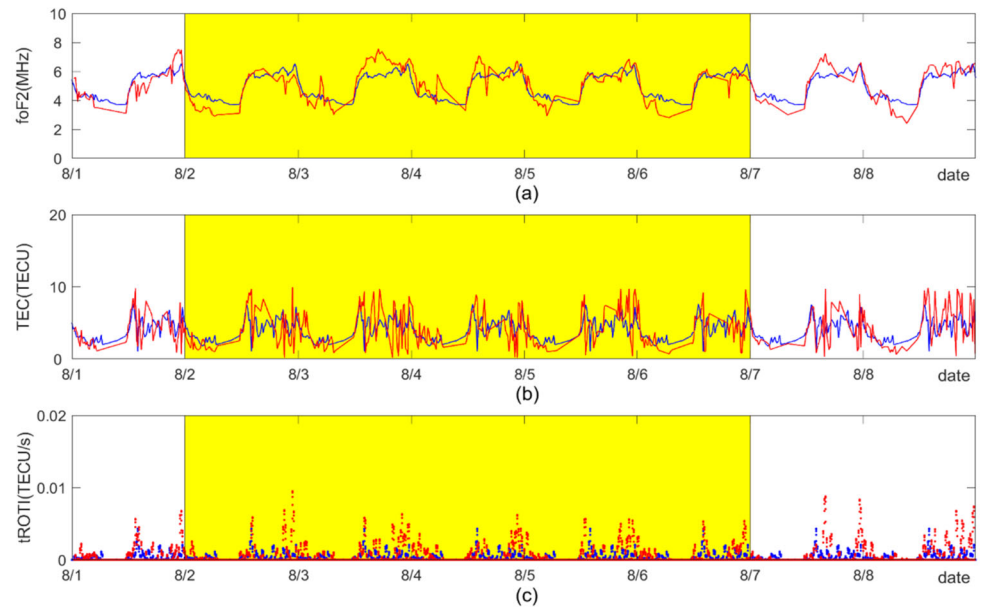


**Fig. 13** Ionosphere foF2 and TEC derived at JI91J station during the HSSWS in 2020 (a) foF2, (b) TEC, and (c) tROTI; solid blue lines represent the reference values of foF2 and TEC, solid red lines represent the observations, and yellow paddings show the period of the HSSWS event



## 4 Conclusion

In this experiment, the high-speed solar wind events from August 1 to 8, 2020 were selected to analyze the ionosphere response. The interplanetary magnetic field and the geomagnetic indices experienced abnormal changes successively from August 2. They returned to normal on August 4.

The ground-based GNSS data indicate that TEC and ROTI in different regions generally increased. The most affected area was the European–African continent during this solar wind event, and the ionosphere TEC increased by 12%. The region with the most significant TEC increase rate of approximately 68% is near 20° E and 35° S. The ROTI value

in high-latitude areas can be six to seven times that in low-latitude areas. The largest disturbance occurred at Nril station, and the ROTI was 4.92 TECU/min. The occurrence rate of ROTI > 0.5 in high latitudes can reach approximately 54%.

The electron density of the topside ionosphere initially increased and then decreased, and eventually returned to normal over time. The electron density increased to its peak on August 3, with a growth rate of 15%. The most dramatic change in the topside ionosphere occurred at 81.1° E and 19.4° N on August 6. It was nearly four times as much as that during the geomagnetic quiet period. The data of in-situ measurements indicate that the region with ionosphere above 460 km and most affected by this HSSWS event was

**Fig. 14** Ionosphere foF2 and TEC derived from LM42B station during the HSSWS in 2020 (a) foF2, (b) TEC, and (c) tROTI; solid blue lines represent the reference values of foF2 and TEC, solid red lines represent the observations, and yellow paddings show the period of the HSSWS event

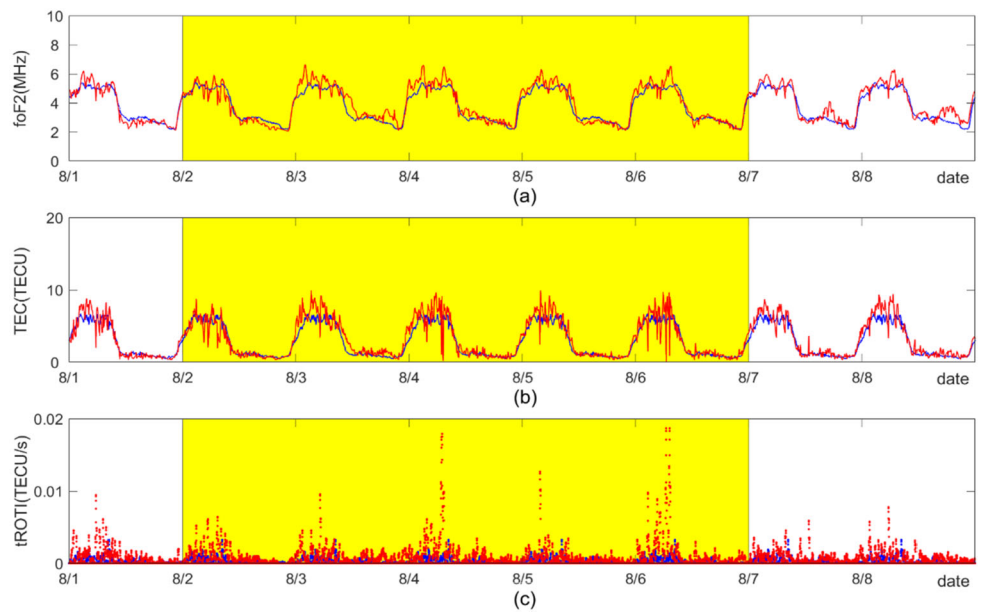


**Fig. 15** Ionosphere foF2 and TEC derived from HE13N station during the HSSWS in 2020 (a) foF2, (b) TEC, and (c) tROTI; solid blue lines represent the reference values of foF2 and TEC, solid red lines represent the observations, and yellow paddings show the period of the HSSWS event

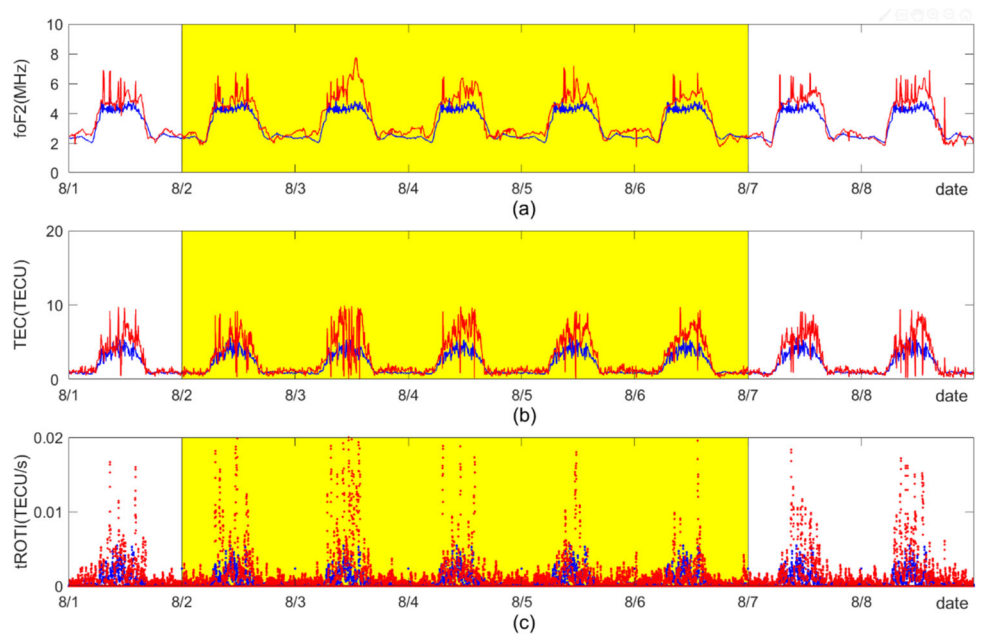


**Table 3** Statistics of ionosphere foF2 and TEC over ionosonde stations

Stations	Average bias between FoF2 and reference values (MHz)	Average bias between TEC and reference values (TECU)	Average variation rate of FoF2 (%)	Average variation rate of TEC (%)
AT138	0.29	0.25	7	9
PRJ18	-0.05	-0.43	-2	-10
J191J	-0.08	-0.05	-2	-2
LM42B	0.16	0.29	4	12
HE13N	0.45	0.78	12	32

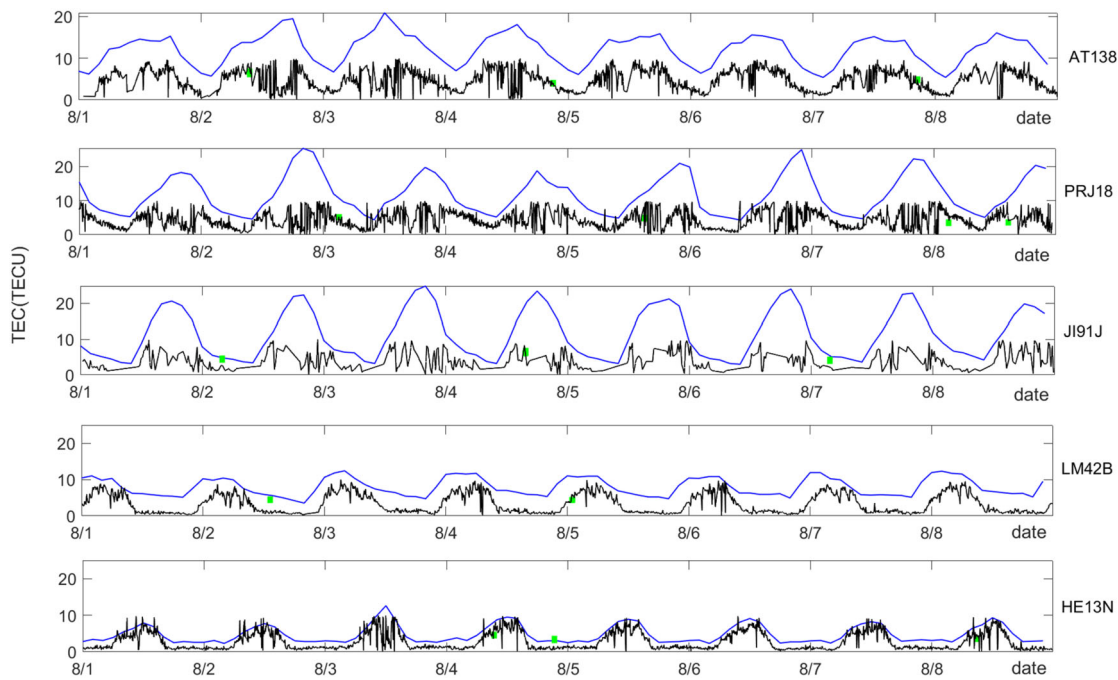


**Fig. 16** Ionosphere TEC changes over ionosonde stations during HSSWS in 2020; solid blue lines and black lines represent the GNSS TEC and ionosonde TEC, respectively, and solid green squares represent SWARM TEC

the European–African continent. The electron density was four to five times higher than that of the geomagnetic quiet period. According to the LEO TEC technology, the top-side ionosphere TEC and ROTI increased evidently during HSSWS.

The lower ionosphere data of the F2 layer obtained through the ionosonde stations also had an increased TEC disturbance. However, the positive and negative disturbances of the TEC and foF2 parameters occurred. During the HSSWS, the most affected station was located in the European–African continent. The increase rate of the HE13N station and AT138 station reached 32% and 9%, respectively. The ionosphere disturbance at low-latitude stations tended to weaken. In addition, the ROTI of ionosonde stations became significantly larger when the GNSS TEC increased.

The comparative result of the ionosphere statistics of the three types of data indicates that each type of data has different characteristics in measuring the number of electrons. They can complement each other to provide a more comprehensive understanding of the ionosphere response under the HSSWS event.

**Funding** This work was supported by the National Natural Science Foundation of China (Grant number 41977415).

**Publisher's Note** Springer Nature remains neutral with regard to jurisdictional claims in published maps and institutional affiliations.

## References

- Beutler, G., Rothacher, M., Schaer, S., et al.: *Adv. Space Res.* **23**, 631 (1999). [https://doi.org/10.1016/S0273-1177\(99\)00160-X](https://doi.org/10.1016/S0273-1177(99)00160-X)
- Bu, X., Luo, B., Liu, S., et al.: *Chin. J. Geophys.* **62**, 462 (2019). <http://www.geophy.cn/CN/10.6038/cjg2019M0570>
- Jin, R., Jin, S., Feng, G.: *GPS Solut.* **16**, 541 (2012). <https://doi.org/10.1007/s10291-012-0279-3>
- Krieger, A.S., Timothy, A.F., Roelof, E.C.: *Sol. Phys.* **29**, 505 (1973). <https://doi.org/10.1007/BF00150828>
- Liou, K., Han, D., Yang, H.: *Terr. Atmos. Ocean. Sci.* **24**, 183 (2013). [https://doi.org/10.3319/TAO.2012.09.11.01\(SEC\)](https://doi.org/10.3319/TAO.2012.09.11.01(SEC))
- Liu, Y., Xu, J., Xu, L., et al.: *Chin. J. Geophys.* **58**, 12 (2015). <http://www.geophy.cn/CN/10.6038/cjg20150102>
- Liu, Y., Li, Z., Fu, L., et al.: *IEEE Access* **7**, 29788 (2019). <https://doi.org/10.1109/ACCESS.2019.2897793>
- Liu, J., Wang, C., Wang, P., et al.: *Astrophys. J.* **891**, 162 (2020). <https://doi.org/10.3847/1538-4357/ab722b>
- Matamba, T.M., Habarulema, J.B.: *Adv. Space Res.* **67**, 777 (2020). <https://doi.org/10.1016/j.asr.2020.10.034>
- Molina, M.G., Dasso, S., Mansilla, G., et al.: *Sol. Phys.* **295**, 173 (2020). <https://doi.org/10.1007/s11207-020-01728-7>
- Nolte, J.T., Krieger, A.S., Timothy, A.F., et al.: *Sol. Phys.* **46**, 303 (1976). <https://doi.org/10.1007/BF00149859>
- Pi, X., Mannucci, A.J., Lindqwister, U.J., et al.: *Geophys. Res. Lett.* **24**, 2283 (1997). <https://doi.org/10.1029/97GL02273>
- Ren, D., Lei, J., Zhou, S., et al.: *Space Weather* **18**, 1542 (2020). <https://doi.org/10.1029/2020SW002480>
- Rodríguez-Zuluaga, J., Radicella, S.M., Nava, B., et al.: *J. Geophys. Res.* **121**, 11528 (2016). <https://doi.org/10.1002/2016JA022539>
- Sulungu, E.D., Uiso, C.: *J. Environ. Eng.* **3**, 103 (2019). <https://doi.org/10.11648/j.ajese.20190304.16>
- Tsurutani, B.T., Lakhina, G.S., Sen, A., et al.: *J. Geophys. Res.* **123**, 2458 (2018). <https://doi.org/10.1002/2017JA024203>

- Watson, C., Jayachandran, P.T., MacDougall, J.W.: J. Geophys. Res. **121**, 9030 (2016). <https://doi.org/10.1002/2016JA022937>
- Zakharenkova, I., Astafyeva, E.: J. Geophys. Res. **120**, 807 (2014). <https://doi.org/10.1002/2014JA020330>
- Zaourar, N., Amory-Mazaudier, C., Fleury, R.: Adv. Space Res. **59**, 2229 (2017). <https://doi.org/10.1016/j.asr.2017.01.048>